An investigation of the spot profiles in transmission electron diffraction from Langmuir-Blodgett films of aliphatic chain compounds

I.R. Peterson, R. Steitz, H. Krug, I. Voigt-Martin

Classification
Physics Abstracts
61.70 — 68.55 — 61.14 — 61.50K — 07.80 — 05.50 — 03.40

An investigation of the spot profiles in transmission electron diffraction from Langmuir-Blodgett films of aliphatic chain compounds

I. R. Peterson, R. Steitz, H. Krug and I. Voigt-Martin

Institut für Physikalische Chemie, Johannes Gutenberg Universität, Jakob Welder Weg. 11, D6500 Mainz, F.R.G.

(*Reçu le 13 septembre 1989, révisé le 5 janvier 1990, accepté le 17 janvier 1990*)

Résumé. — Les profils des réflexions de Bragg provenant d'une couche de Langmuir-Blodgett sont dérivés selon trois modèles plausibles de l'organisation moléculaire : une phase polycristalline à ordre orientationnel de longue portée ; un paracristal possédant une densité de défauts ponctuels qui ne dérangent pas les rangs moléculaires ; et une phase smectique hexatique du type Nelson et Halperin dans la limite « Debye-Hückel » où les interactions entre les dislocations sont faibles. Les trois prévisions sont nettement différentes l'une de l'autre. Des résultats expérimentaux à température ambiante sont présentés pour des couches de Langmuir-Blodgett fabriquées à partir d'un lipide, le DMPE, et du sel de cadmium d'un acide gras insaturé, le 22-tricosénoïque. Seule la théorie de Nelson et Halperin donne un accord satisfaisant, malgré des déviations qu'on peut attribuer à des défauts du type paracristallin ou à un comportement non ergodique de la couche. On en déduit des densités de dislocations de l'ordre de 10^{-4} à 10^{-5} par molécule.

Abstract. — The profiles of the transmission diffraction spots from a Langmuir-Blodgett film of aliphatic chain compound are derived from three plausible models of molecular organisation : a polycrystalline phase with long-range orientational order ; a paracrystal possessing a density of point defects which do not interrupt the lattice rows ; and a Nelson and Halperin hexatic smectic phase in the « Debye-Hückel » limit of weakly-interacting dislocations. The three resulting predictions are distinctly different. Experimental results are presented for the room-temperature diffraction patterns from Langmuir-Blodgett films of a lipid, DMPE, and the cadmium soap of a fatty acid, 22-tricosenoic. Only the Nelson and Halperin theory gives a satisfactory fit, although there are deviations attributable to paracrystal-type defects or to non-ergodic behaviour of the layer. Dislocation densities of between 10^{-4} and 10^{-5} per molecule are deduced.

1. Introduction.

Electron diffraction has been used since the 1930s [1, 2] to investigate the molecular packing on the nanometre scale in the organic films deposited by the Langmuir-Blodgett (LB) technique. The diffraction patterns obtained contain a number of discrete spots, which in these and subsequent studies [3-7] have been interpreted in terms of a crystalline packing of the molecules.

While the crystalline hypothesis has the advantage that many such materials are known and that the theory of their diffraction patterns is well understood, it has never been completely satisfying as an explanation of LB film diffraction results. Ideal crystals produce sharp diffraction spots, even in the presence of thermal disorder : the effect of an equilibrium distribution of phonons is to reduce the peak intensity (by the Debye-Waller factor) and to introduce a smooth scattering background, without any peak broadening [8]. In contrast, the reflections from LB films generally display peak broadening as well as arcing, a fact which was first brought to attention by Fischer and Sackmann [9], and subsequently by Garoff *et al.* [10].

In the usual case of a polycrystal, the distribution of grain orientations is isotropic, and the diffraction pattern consists of Debye-Scherrer rings. In contrast, reflection high-energy electron diffraction studies of LB films typically show a fibre pattern. This is normally considered to arise from polycrystalline aggregates with statistical fluctuations about a preferred molecular orientation (the fibre axis) [11].

An additional feature of the diffraction patterns from LB films is that the number of reflections is much smaller than that obtained from single crystals of molecularly similar materials [11]. The missing diffraction spots are those of high order. This may also be ascribed to fluctuations in molecular orientation or position, and indicates that their correlation length is small.

The observation of localised peaks of diffraction intensity in spite of these fluctuations of molecular positions and orientations indicates the presence of orientational order of the lattice extending over much larger distances. Information about this can be obtained more conveniently using polarised microscopy. In recent studies of LB films of the fatty acids and soaps [12], textures typical of hexatic smectic mesophases have been reported. These are characterised by a continuous variation of the preferred optical axes at almost all points. At some points, the orientation of the optical axes changes much more rapidly than elsewhere, forming a pattern of lines similar in some respects to grain boundaries. However they do not enclose « domains » of constant orientation, and most are open (i.e., have two ends), without *Y*-junctions. The change of orientation across these lines is equal to 60° within experimental error, and the resulting diffraction patterns which can be indexed as arising from grains differing in orientations by 60° have been ascribed to « hexagonal twinning » [13]. The ends of the lines of discontinuity have been identified as the orientational defect structures known as disclinations [14-16]. Taken together, the observed details of the texture imply complete loss of translational correlation within optically-resolved separations in all directions within the monolayer plane (as in a liquid), while correlations of the lattice orientation are retained to much greater distances, typically tens to hundreds of μm.

It is of more than academic interest to understand the physical basis for the differences between crystalline and smectic behaviour, because in attempts to apply LB films in practical applications, characteristic smectic textures appear to be responsible for many of the departures from desired behaviour [17, 18]. Moreover, one of the commonly expressed aims of LB research is « molecular electronics » [19], where the local environment of each and every molecule is expected to be important. Since the diffraction pattern is readily accessible and produces distinctly different results with crystalline and smectic materials, it seems reasonable to test theories of molecular order in these phases against their predictions of the diffraction pattern.

It is well known that the interaction of electrons with matter is very strong, and the possibility of multiple diffraction (or dynamical scattering) must be very seriously considered in any detailed correlation of a structure and the resulting diffraction pattern. However Dorset has shown [20] that the single-scattering (kinematic) approximation holds well for crystalline sample thicknesses of less than 7 nm, while in recent work with liquid crystal

polymers it has been shown both experimentally [21] and theoretically [22] that the kinematic approximation is valid for sample thicknesses of a few tens of nm. Hence for the case of organic monolayers thinner than 3 nm supported on an amorphous substrate less than 20 nm thick the kinematic theory is quite adequate.

In the present work, three possible models of molecular organisation are analysed using the kinematic approximation. Each is plausible, and has at some time been proposed seriously to describe the order in smectics or LB films. The first is a polycrystalline texture, in which regions of defect-free crystal with constant orientation (« grains ») are separated by sharp boundaries. This is the model implied by the normal nomenclature used in diffraction studies, which was developed for inorganic materials. In order to make this model conform with the observed long-range orientational order in LB films, it is necessary to assume that, as a result of some mechanism, the orientations of neighbouring grains are highly correlated.

The second is the Nelson and Halperin (NH) theory of hexatic smectic mesophases, which has in previous papers [14, 15, 23] been proposed as a model for fatty acid LB organisation. Unfortunately, although Nelson and Halperin have extensively analysed the expected elastic and thermodynamic properties of these phases [24-27], and have derived functions related to scattering, nowhere in their work do they directly derive the diffraction pattern. This oversight is rectified in the present paper for the physically plausible « Debye-Hückel » limit of weakly interacting dislocations.

The third model is a paracrystalline model of disorder [28]. Historically, the paracrystal concept proposed by Hosemann and Bagchi was the first attempt to explain the diffraction spot broadening encountered with many organic materials, and was developed from plausible models of lattice disorder in one dimension [29], assuming that, unlike the case of inorganic materials [30], dislocations can be ignored. Unfortunately for this theory, dislocations have recently been observed directly in organic thin films [21], and there is no theoretical justification for « Gaussian error propagation » in two or more dimensions. The original formulation has been ably and definitively criticised by Brämer and Ruland [31], and by Crist and Cohen [32]. Although there are sufficient free parameters in the theory to fit the variation of spot widths observed from many organic materials, they pointed out that the predicted small-angle scattering does not correspond to experiment. Hence there are no grounds for believing that the parameters extracted for a particular material provide any insight into its local molecular organisation.

Although Hosemann's version of paracrystal theory can therefore no longer be taken at face value, it does address a real phenomenon which is ignored in the NH theory. Hosemann considered line broadening to be due to defects such as vacancies, chain kinks, impurities, random crosslinks, or regions of different but near-commensurate molecular packing, whose overall Burgers vector is zero, and it is clear that defects of this sort exist. The NH model treats only the effects due to dislocations.

The methods used in the NH theory indicate how the underlying physical assumptions of the Hosemann model might be treated correctly in two dimensions. The defective assumption of « Gaussian error propagation » must be replaced by the self-evident one of mechanical equilibrium. The resulting analysis of the modified model is presented here. As in the NH model, the lattice is assumed to be mechanically isotropic, an assumption which is exact for hcp packing.

Finally, the diffraction patterns predicted by each of these models have been compared to experimental results. Two monolayer-forming substances were investigated, in case a particular substance should turn out not to be typical. For this reason also, an attempt was made to select substances from different categories, although the selection could not be entirely at random, because NH model predictions are only available if the lattice is

hexagonal close packed. Two substances were chosen : firstly, a biological lipid, dimyristoyl phosphatidyl ethanolamine (DMPE) ; and secondly, the cadmium soap of a long-chain unsaturated fatty acid, 22-tricosenoic acid (Cd 22TA). Molecules of both substances are similar in possessing long aliphatic chains as an important structural feature, although the number of chains per molecule and the details of the hydrophilic headgroups are quite different.

Provided that the predictions of the three models differ by more than the experimental error, then agreement of one of the models with the measured value can be taken as a criterion of validity. Conversely, if the prediction of a given model disagrees with the measured value by more than the experimental error, then this can be taken as grounds for rejecting it. However in this case it must also be considered whether the model can be plausibly modified to bring its predictions into line with observation.

2. Experimental.

The LB deposition was performed using either a Lauda type FW-1 analog-controlled trough or a Nima type TKB 2410 A computer-controlled trough. The subphase water was purified using a Milli-Q recycling deioniser/active charcoal/filter unit fed with distilled water. For the deposition of cadmium tricosenoate, 1.4×10^{-4} M $CdCl_2$ and 10^{-4} M $NaHCO_3$, both Merck p.a. grade, were added. Spreading solutions of both DMPE and 22-tricosenoic acid of approximately 1 g/l concentration were prepared in freshly purchased p.a. grade chloroform. The 22-tricosenoic acid was synthesised as described previously [33] and was found using NMR to contain 1.5 % of the 21-isomer. The DMPE was purchased from Merck and was used without further purification.

Hydrophilic Formvar-coated electron microscope grids were prepared using a technique described previously [34, 35]. Using an optical interference technique described elsewhere [36] the thickness of the Formvar film was determined to be typically less than 20 nm. These were coated with monolayers of DMPE at a surface pressure of 27 or 39 mN/m, or with cadmium tricosenoate at a surface pressure of 35 mN/m, both at a withdrawal speed of 83 μm/s and temperature of 20 °C.

It is well-known that radiation damage poses a serious problem in electron microscopic studies of materials consisting largely of aliphatic chains [37-39]. Beam damage leads initially to spot broadening and, in extreme cases, the lattice expands measurably, inducing a phase change from an orthorhombic to a hexagonal subcell packing [40, 41]. For this reason the electron diffraction patterns were all obtained under low-dose conditions. Changes in the diffraction patterns were detectable after four times the standard exposure.

Transmission electron diffraction patterns from the Formvar-coated grids were obtained in a Philips EM300 electron microscope at normal beam incidence and calibrated against an evaporated thallium (I) chloride sample. The accelerating voltage in all cases was 80 kV. The sample area contributing to the diffraction pattern corresponded to one hole of an electron microscope grid, i.e. approximately 100 μm in diameter. The images were recorded on Ilford PANF film and developed using Kodak D19 developer for 5 min. Two-dimensional scans of optical density of the resulting negative were obtained using a Plumbicon camera whose output was digitised and stored in computer memory as a 512×512 array of 8-bit brightness values.

The coordinates of the undeviated beam centre were determined by averaging those of the six (100) diffraction peaks. The small linear shift in baseline caused by nonuniform illumination of the negative was subtracted, as was the circularly-symmetrical scattering background from the Formvar substrate.

All processing subsequent to background subtraction involved least-squares fitting to theoretical peak profiles. Almost all previous studies have investigated the fit to the one-dimensional Lorentz profile $(1 + \alpha r^2)^{-1}$. However in appendix D it is shown that in two dimensions, exponentially decaying correlations lead to a $(1 + \alpha r^2)^{-1.5}$ behaviour. A variable exponent was therefore included in the program, with the advantage that the Gaussian case is given by the limit of large exponent.

To obtain a contour plot, the digitised intensity values cannot be used directly because they are not defined at a continuum of points. To derive the plot of figure 2, the background-corrected values were convolved with a smoothing function $S(x, y)$ defined by :

$$\left.\begin{aligned} S(x, y) &= [\cos(\pi x/4) \cdot \cos(\pi y/4)]^2 \quad \text{when } |x| < 2 \text{ and } |y| < 2 \\ &= 0 \qquad\qquad\qquad\qquad\qquad\quad \text{otherwise,} \end{aligned}\right\} \tag{1}$$

where the coordinates x and y are expressed in pixel units. The resulting intensities at the pixel centres differ minimally from the original measurements, but in addition are defined at all intermediate points with continuous first derivatives, so that the directions of the contour lines vary smoothly. The smoothed function was not used in any of the model fitting procedures.

The histograms of figure 3 were obtained by summing normalised Gaussians for each peak measured (18 in each case) with a mean equal to the observed axis ratio and a standard deviation equal to that for the measurement. To determine the aspect ratio of a peak, all the pixel values immediately surrounding it in the range from 20 % to 100 % peak height were least-squares fitted to the theoretical function with the intermediate value 5 for the exponent. To determine its standard deviation, the variances due to Gaussian fluctuations in each pixel were added, assuming essentially linear dependence on each of the pixel values. The standard deviation of each pixel was conservatively taken equal to the entire rms difference between the measured values and the best fit function, i.e., assuming no systematic error.

To determine which profile was a better fit to the (100) reflections (Fig. 5), the least-squares fit routine considered all pixel values within a square of side equal to three times the typical full-width half-maximum (FWHM). The goodness-of-fit criterion was taken to be the value of rms error. Due to the low-dose exposure, the silver density in the film was small. No evidence for saturation of the film response was observed, and in consequence no compensation for nonlinearity was applied. It should be noted that any residual nonlinearity will tend to favour the Lorentzian fit relative to the Gaussian.

In tables I and II, each value of radial peak width FWHM given is the mean of the six values FWHM_i from the corresponding sample. The value quoted for its standard deviation σ was calculated from the $N = 6$ values using the usual statistical formula :

$$\sigma = \sqrt{\Sigma(\text{FWHM}_i - \text{FWHM})^2/N/(N-1)}\,. \tag{2}$$

3. Results.

3.1 THEORETICAL. — The theoretical spot profiles for the polycrystalline, Nelson-Halperin (NH) and paracrystal models are derived in appendices A, B and C respectively. The predictions can be classified into three distinct aspects, concerning the aspect ratio of the spot contour, the profile of radial sections through the spot, and the relationship between the spot widths of different diffraction order, respectively.

Contour Aspect Ratio. The most readily measurable feature of the spot contour, or locus of points with a given scattering intensity, is its aspect ratio, defined as the ratio of tangential to radial width. All three models predict that the value should be independent of the particular

intensity. The polycrystalline model gives 1, the NH model predicts $\sqrt{3}$, while the paracrystal model can give values larger or smaller than unity depending on the balance between isotropic and anisotropic defects in the lattice.

Profile. The radial spot profile is Gaussian for the NH model, Lorentzian for the polycrystal, and power law for the paracrystal.

Spot Width Variation. Although all three lead to spot broadening, the FWHM (full-width half-maximum) spot width is independent of diffraction order in the polycrystalline case and proportional to diffraction order in the NH case. In the paracrystal case there is a critical distance from the origin, inside of which the spot FWHM is zero, and outside of which there are no spots at all.

Hence all three predictions are well defined and distinctly different, an ideal situation for an experimental test.

3.2 EXPERIMENTAL RESULTS. — TED negatives were obtained from 3 DMPE samples and 3 Cd 22TA samples. Figures 1 shows all the diffraction patterns of the two types. When measured conventionally by optical comparison with a graduated scale the d-spacings of all first-order reflections were the same and equal to 0.416 ± 0.008 nm, corresponding to hcp packing with unit cell vector equal to 0.481 ± 0.010 nm. It can be seen that the first-order (100) spots are oval in shape, with tangential and radial symmetry, and tangential dimensions somewhat larger than radial. Faint (110) spots are visible, but higher order diffraction spots are missing.

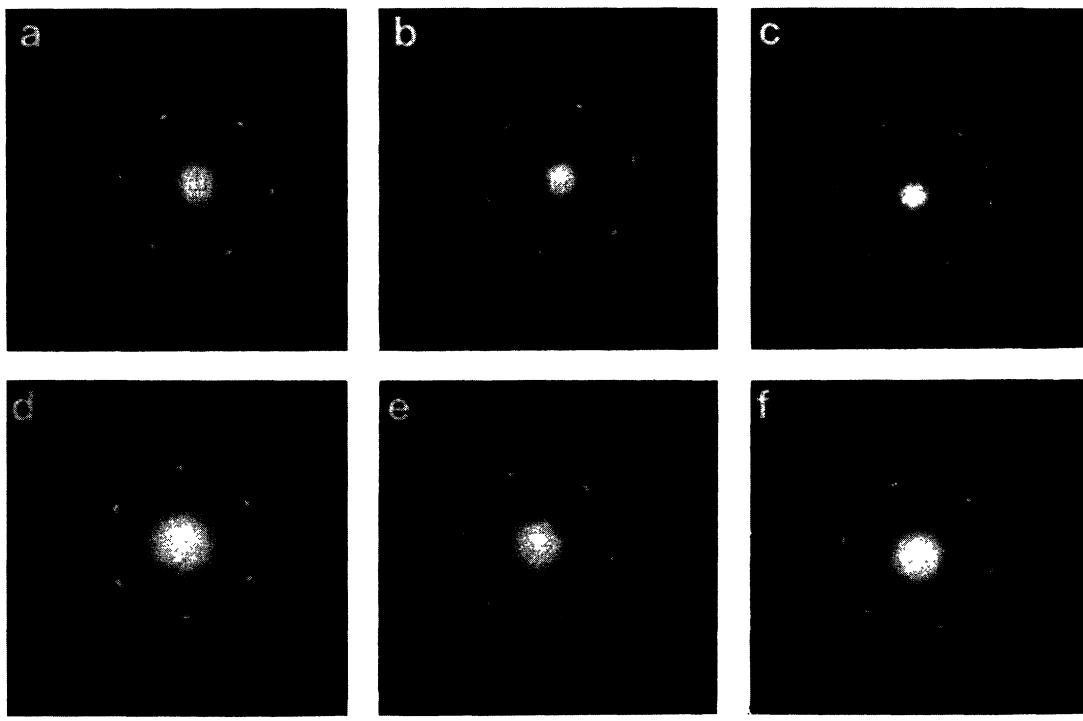

Fig. 1. — Transmission electron diffraction pictures from all of the samples : Cd 22-TA : (a) 55879 (b) 55880 (c) 55882 ; DMPE : (d) 55499 (e) 55518 (f) 55775.

The negatives were digitised and stored on diskette as a file of 512 × 512 bytes for further analysis. The contour plot of figure 2 was obtained from one of the (100) peaks of the figure 1a negative as described in section 2.

Monolayers on Formvar substrates of the cadmium soaps of the fatty acids [42] and DMPE [43] have been previously reported to display hcp molecular packing. However, just as reported in reference [44], the intensities of the six (100) spots were found to fluctuate by more than 20 %, their radial and tangential widths by more than 10 % and their d-spacings by 2 %. These fluctuations are greater than the maximum probable error in the measurements.

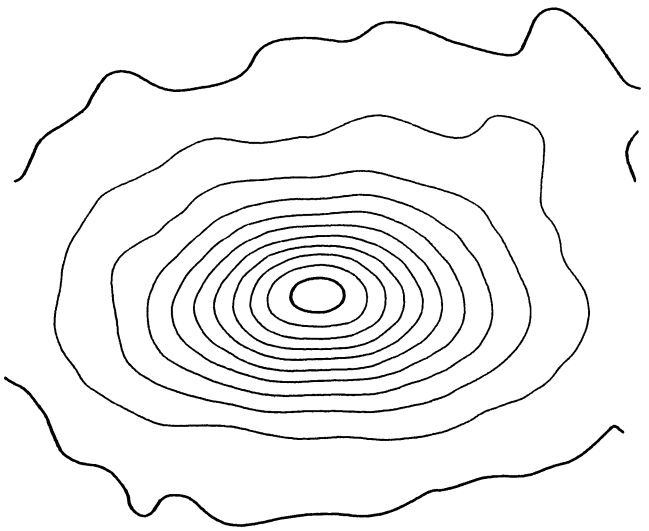

Fig. 2. — Contour plot of one of the (100) spots of the DMPE diffraction picture shown in figure 1, after digitisation, background subtraction, and convolution. The undeflected beam is in the direction of the bottom of the page.

Figure 3 shows histograms plotted for the (100) and (110) peaks of both DMPE and Cd 22-TA samples as described in section 2. In each category there are three samples with six spots each, giving a total of eighteen peaks for each histogram. The values observed are marked by symbols plotted on the curves, with different symbols indicating different samples. For the (100) spots, the values are clustered near $\sqrt{3}$, the lowest values being within experimental error of $\sqrt{3}$ but the highest values significantly larger. The spread of values for the peaks from the one sample was considerably smaller than the spread between samples.

Fitting to the (110) peaks was difficult, probably related to the fact that in the best case the peak was only a factor of 5 higher than the noise, and two of the DMPE (110) peaks could not be distinguished from noise. When the best-fit algorithm was allowed simultaneously to vary the peak coordinates, amplitude, and widths, the result in 80 % of cases was very slow convergence to a completely implausible best fit. The values plotted were obtained by fixing the positions at points on the hcp lattice found to be the best fit to the (100) peak positions, and the amplitude to correspond to the largest pixel value encountered. The spread in the aspect ratios for these peaks, even within the one sample, was significantly larger than the computed standard deviations.

Figure 4 shows the pixel values along a radial cut through the peak of figure 2 as a discontinuous, piecewise constant function, superimposed upon the best-fit Gaussian

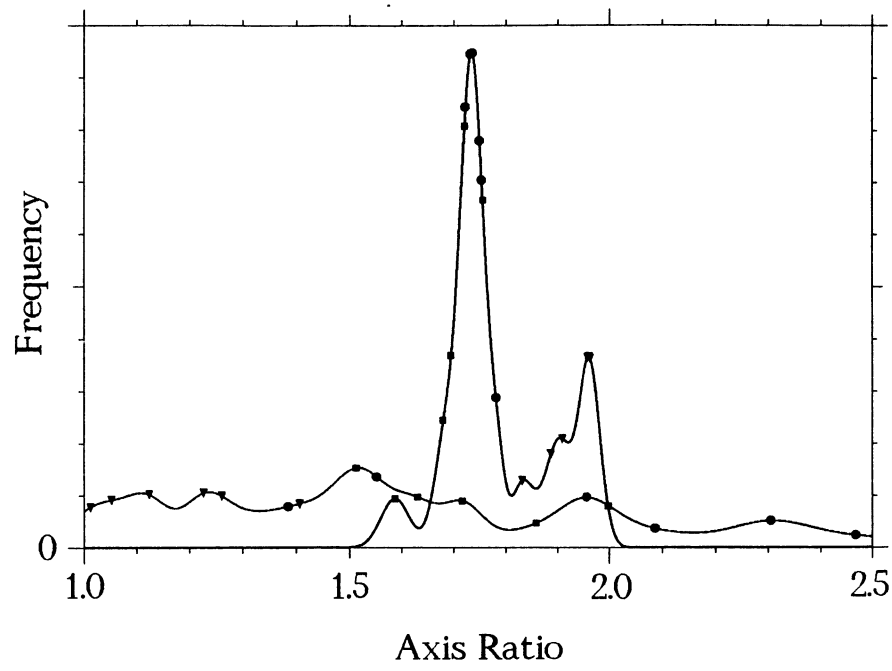

a)

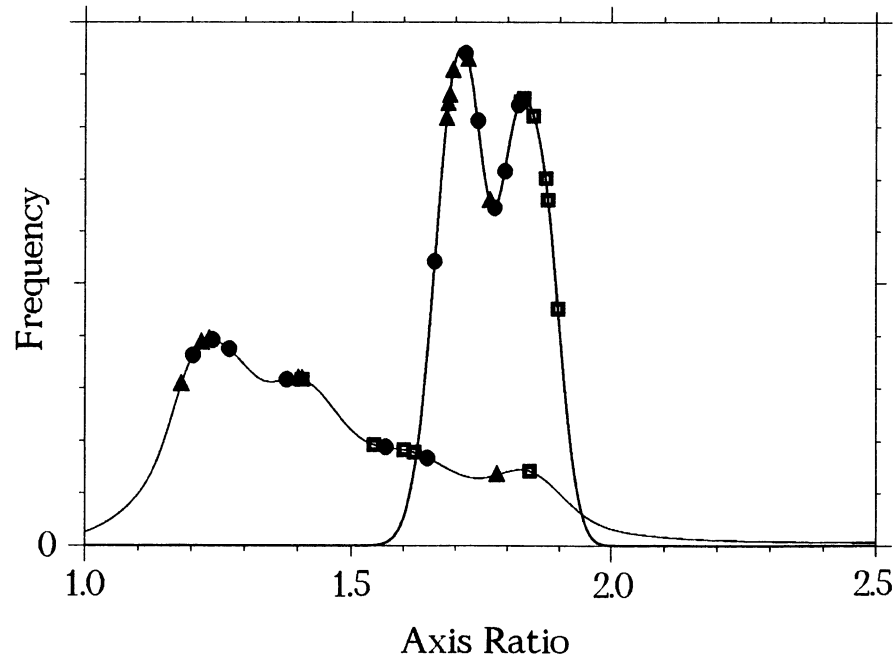

b)

Fig. 3. — Histograms formed by adding normalised Gaussians for each best-fit major/minor axis ratio with a standard deviation equal to that of the measurement. The frequency scale is arbitrary but the same for both curves on the one plot. (a) First-order and second-order peaks for the three cadmium 22-tricosenoate samples. (b) First-order and second-order peaks for the three DMPE samples.

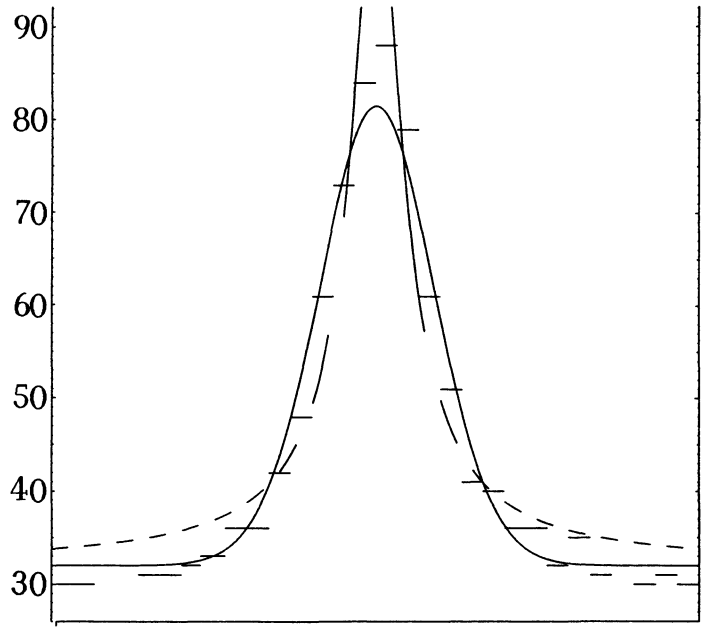

Fig. 4. — Radial cross-section plot of the (100) spot of the DMPE diffraction picture whose contour is shown in figure 2, represented as piecewise constant pixel values, together with best-fit Gaussian and Lorentzian functions (solid curve, and broken curve, respectively).

(exponent 100) and Lorentzian (exponent 1.5). In both cases the background value was assumed fixed at 32 by the background subtraction program, but the centre position, amplitude, radial FWHM and tangential FWHM were allowed to vary as part of the fit. It can be seen that the Gaussian overestimates the FWHM and underestimates the amplitude, while the Lorentzian underestimates the FWHM and overestimates the amplitude. This was the case in essentially all the peaks analysed. When the exponent was also allowed to vary, the best fit in all cases was found for intermediate values of the exponent. In particular, the one-dimensional Lorentzian (exponent unity) was never a better fit.

Figure 5 shows the residual error for the fit to the Gaussian *versus* the residual error for the fit to the Lorentzian, plotted as the rms value (i.e., the square root of the sum of squared residuals divided by the number of points). The values were in all cases significantly larger than the background noise, indicating the presence of systematic error. While individual cases can be found where the Gaussian or the Lorentzian is a better fit, overall this test does not favour either the polycrystalline or the NH model. However the width of the best-fit Lorentzian was in all cases much larger than the film or equipment resolution, so that pure negative power-law behaviour as predicted by the paracrystal model is completely incompatible with the observations.

Table I gives the fit parameters relevant to the polycrystalline model for the third area of comparison, namely, the variation with diffraction order of the peak width of the best Lorentzian fit to the radial profile. With both 22-TA and DMPE the (200) diffraction peaks could not be detected, so the comparison is essentially between the (100) reflections closest to the undiffracted spot, and the (110) reflections whose d-spacing is smaller by a factor of $\sqrt{3}$. According to the polycrystalline model, the peak width should be independent of diffraction order, so that the quantity in the second-last column of table I should be unity.

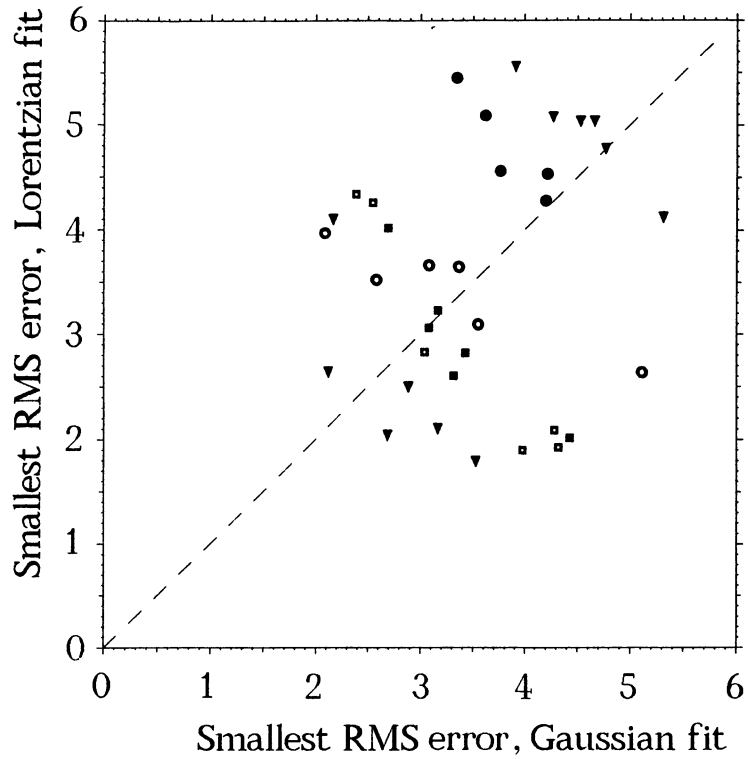

Fig. 5. — Plot of the best-fit Gaussian error *versus* the best-fit Lorentzian error for all 36 first-order diffraction spot measured. The units are the those of the video digitiser, and correspond to approximately 1 % of the peak height.

Table I. — *Peak width variation with diffraction order and extraction of physical parameters on the polycrystalline model.*

Monolayer Material & Sample	FWHM ± σ of best-fit Lorentzian (average for six peaks)		$\frac{FWHM_{110}}{FWHM_{100}} \pm \sigma$	Characteristic domain size ξ, nm
	(100) Peaks, cycles.μm^{-1}	(110) Peaks cycles.μm^{-1}		
Cd 22-TA				
55 879	86.1 ± 3.7	166 ± 29	1.94 ± 0.34	2.83
55 880	74.2 ± 2.7	191 ± 131	2.58 ± 0.43	3.29
55 882	60.7 ± 1.7	305 ± 38	5.03 ± 1.52	4.02
DMPE				
55 499	65.0 ± 4.4	164 ± 52	2.52 ± 0.75	3.75
55 518	49.5 ± 3.9	197 ± 70	3.99 ± 1.42	4.93
55 775	58.3 ± 3.0	286 ± 78	4.91 ± 1.34	4.19

However the values for this ratio appear to be systematically higher, by an amount larger than the probable error. All values lie outside the $\pm 2\,\sigma$ error bars, and one lies outside $\pm 3\,\sigma$.

The characteristic domain size ξ was calculated from the best-fit FWHM using equation (A.3).

To test the NH model in the third area of comparison, a Gaussian is fitted to the diffraction spot profiles, and table II gives the resulting best-fit parameters. On this model the peak width should be proportional to the scattering vector Q of the diffraction spot, so that in column 4 the width ratio divided by the scattering vector ratio should be unity. In fact of the entries in this column, two lie within the $\pm\,\sigma$ error bars and all lie within $\pm 2\,\sigma$.

The dislocation density in column 5 of table II is deduced from equation (B.12) using the measured values of radial FWHM. In comparison with table I, it can be seen that the number of dislocations required to explain the spot broadening on the NH model is much smaller than the number of domains required on the polycrystalline model.

Table II. — *Peak width variation with diffraction order and extraction of physical parameters on the Nelson and Halperin model.*

Monolayer Material & Sample	FWHM $\pm\,\sigma$ of best-fit Gaussian (average for six peaks)		$\frac{1}{\sqrt{3}} \cdot \frac{\text{FWHM}_{110}}{\text{FWHM}_{100}}$	Normalised dislocation density $\tilde{n}$ /molecule
	(100) Peaks, cycles.μm^{-1}	(110) Peaks cycles.μm^{-1}		
Cd 22-TA				
55 879	177 ± 7	253 ± 31	0.83 ± 0.10	9.2×10^{-5}
55 880	153 ± 5	281 ± 36	1.06 ± 0.14	6.9×10^{-5}
55 882	121 ± 3	318 ± 74	1.52 ± 0.35	4.3×10^{-5}
DMPE				
55 499	137 ± 7	274 ± 64	1.15 ± 0.66	5.5×10^{-5}
55 518	114 ± 7	309 ± 75	1.57 ± 0.38	3.8×10^{-5}
55 775	121 ± 5	403 ± 92	1.90 ± 0.45	4.3×10^{-5}

4. Discussion.

4.1 THEORETICAL. — Although Nelson and Halperin do not derive an expression for the scattering function, they do derive the asymptotic expression for a related function $C_q(R)$ as R tends to infinity [26]. $C_q(R)$ is the Fourier transform of the peak of the Patterson function centred at the real-space lattice point R, evaluated at one of the six first-order reciprocal lattice points q :

$$C_q(R) \sim \exp(-|R|/\xi^+)\,. \tag{3}$$

This would seem to imply a Lorentzian profile for the diffraction spots, as opposed to the Gaussian law derived in appendix B. The discrepancy may be traced to the evaluation of the integral (B.8) where the following approximation is made :

$$\sin(\pi|Q||Y|\cos\varphi) \approx \pi|Q||Y|\cos\varphi\,. \tag{4}$$

This is justified when $|Y|$ is small, i.e. for the inner peaks of the Patterson function corresponding to separations much smaller than the average distance between dislocations. When the approximation is not made, the correct asymptotic form for $C_q(R)$ is obtained. However the outer peaks of the Patterson function are so broad that they merge into one another, and at the observed normalised dislocation densities of roughly 10^{-4}, the detailed asymptotic behaviour of the Patterson peak widths makes little difference to the observable features of the scattering function.

The NH theory is not the first ansatz-free analysis of diffraction line broadening due to dislocations. The theory for bulk media has been treated in several reports [30, 45-48], but the results are distinctly different from the present 2D case. In particular, in equation (B.12), the expected radial diffraction spot FWHM varies with the normalised diameter B of the selected diffraction area, whereas in the three-dimensional case the spot broadening is independent of B. For an infinitely wide film and incident beam, the predicted NH spot diameter diverges. Physically, this is related to the fact that a uniformly spaced linear row of identical dislocations with Burgers vector perpendicular to the row (a symmetrical grain boundary) produces a finite change of orientation but a strain field which decays rapidly to zero. As a consequence, there is no stress field neighbouring the row which might cause other dislocations to move and hence introduce an exponential shielding factor, such as in found in the Debye-Hückel treatment of an electrolyte. On a more fundamental level, the divergence is related to Peierls proof [49] that long range order in two dimensions cannot persist to infinite separations. However, in practice this logarithmic divergence is scarcely noticeable. The smallest feasible value of B is roughly 2×10^4 for a 1 μm-diameter selected diffraction area, and the largest roughly 2×10^6, giving a range of variation of spot size with diffraction aperture of less than 22 %.

The line shape predicted by the NH theory has been described as Gaussian, and this is to a good approximation true. However strictly speaking, it is a Gaussian divided by the square of the distance to the origin. This results in a shift of the spot centre towards the origin, and hence larger d-spacings, with respect to the position for a defect-free lattice.

The NH model is physically incompatible with the polycrystalline model, because they correspond to two completely different ways of organising the dislocations of the crystalline lattice. However the NH model is compatible with the paracrystalline model, which describes the line broadening due to unbound lattice defects of a different type. When both types of defect are present, the resulting spot profile is the convolution of the two individual profiles.

4.2 EXPERIMENTAL. — The broadening of the diffraction peaks is in all cases much higher than any possible limit imposed by the electron microscope. The paracrystal model predicts a power law peak profile, with zero FWHM. Hence it is possible to rule out the paracrystal model, at least in its pure form, and to say that the crystal lattice of the monolayer must contain dislocations. This is the case in the other two models considered : they are either organised in specific configurations, as in the polycrystalline model, or almost randomly distributed, as in the NH model.

It can be seen from figures 2 and 3 that the contour lines are not circular, as would be expected for the polycrystalline model analysed. The observed aspect ratios for the well defined (100) peaks show a sharp clustering in the vicinity of the value of $\sqrt{3}$ predicted by the NH model. This was also the case in an independent study of diffraction spot intensities from monolayers of cadmium soaps of three different fatty acids [44]. The polycrystalline model could perhaps be amended to include a statistical fluctuation of the domain orientation to restore agreement with the experimental findings. It is however difficult to see how such an *ad hoc* modification could account for the observed clustering of the aspect ratios of the (100) peaks.

On the polycrystalline model, the best fit characteristic domain size ξ is of the order of 5 nm, that is to say 10 lattice constants. Now it is known that the density of dislocations along a grain boundary is related to the change of orientation across the boundary. From the diffraction patterns it can be seen that the standard deviation of orientational fluctuation cannot exceed 0.05 radians. The difference in the orientation between two neighbouring domains must on average be less than twice this value, leading to an expected number of dislocations on domain boundaries of order unity. However an initial assumption of the model was that the interior of each domain was strain-free, and efficient shielding of external strains by a grain boundary requires many dislocations. Hence the fit to the polycrystalline model is internally inconsistent.

Since it leads to a contradiction to assume that the boundary of a grain shields its interior from external strains, the notion cannot hold for the present system. On a suitably modified version of the polycrystalline model, therefore, the orientation within a grain is not necessarily constant. As already discussed, the observed long-range orientational order is incompatible with the presence in the films of large-angle grain boundaries. It is well known that low-angle grain boundaries can be resolved into a sequence of widely-spaced dislocations [50]. Hence the polycrystalline model revised to take account of the present experimental findings starts to look very much like the NH model.

A recent paper has reported the direct electron microscope image of a cadmium eicosanoate monolayer showing a roughly-circular region of $\sim 10^3$ molecules free of dislocations or grain boundaries [51]. This is consistent with the present fits to the NH theory, which indicate a defect density of fewer than 1 dislocation per 10^4 molecules, but at variance with the present fits to the polycrystalline model, where in each case the characteristic domain size ξ^2 contains fewer than 10^2 molecules.

The NH theory can provide an explanation for the observed small, but significant, departures of the diffraction peaks from hexagonal symmetry. The divergence of the spot FWHM for infinite aperture size is related to the fact that the strain field from a dislocation decays as r^{-1}, with no cut-off. Dislocations significantly outside the diffraction aperture cause the same strain at each diffracting point, and so do not contribute to spot broadening, but do cause an overall shift in the peak position. Since grain boundaries in a polycrystal effectively isolate each domain from any strain fields in neighbouring regions, the polycrystalline model cannot explain this phenomenon.

The deviations of (100) spot aspect ratio from the NH prediction were in the direction of higher ratios. High aspect ratios were also found in an independent electron diffraction study of stearic acid monolayers [10]. This is the effect expected from a density of disclinations, which are observed in the films but which are not considered in the NH theory. The density of disclinations in monolayers of 22-tricosenoic acid produced in the same laboratory using the same equipment as the present experiments has been elsewhere reported [52] to be of the order of 10 mm^{-2}. A disclination of rotation 60° located 300 μm from the diffraction aperture of diameter 100 μm will result in a maximum relative rotation of the crystalline lattice by 20° from one side to the other, resulting in an increase of the tangential FWHM of an otherwise sharp (100) peak of approximately 0.3 cycles.nm^{-1}. Hence the excess tangential broadening observed in the present work can be readily explained in this way. In a different laboratory, one of the present authors has measured much higher disclination densities, of the order of 1 000 mm^{-2} [53], so that much greater deviations from the « ideal » $\sqrt{3}$ ratio can also be explained. Unfortunately, methods of producing aligned monolayers have not yet been perfected, so that this source of uncertainty cannot yet be eliminated.

Although some of the spot profiles observed in the present work show smaller residual errors for a Gaussian function, others give a better fit to Lorentzian. A better fit to Lorentzian

form for the radial scattering profile was also observed in two previous studies [9, 10], and is incompatible with the « pure » NH theory derived in appendix B. However there appear to be two plausible ways in which the theory could be extended to explain a proportion of non-Gaussian profiles.

Firstly, the existence in LB films of lattice disturbances with zero Burgers vector can scarcely be doubted. Reflection high-energy electron diffraction (RHEED) studies have provided unambiguous evidence for the coexistence of orthorhombic and triclinic aliphatic subcell packings with similar tilt in LB films of pure long-chain acids [12]. It is also clear that impurities are almost always present at the 1 % level, and many authors have proposed that $g^+ g^-$ kinks commonly occur in the chains [54].

A further type of disturbance with zero Burgers vector which is indisputably present is provided by the molecular shape, which does not share the observed macroscopic hexagonal symmetry. In many smectic B phases it has been well established that the diameter of the smallest cylinder which completely contains the Van der Waals surface of one molecule is considerably larger than the measured lattice parameter, indicating that the observed sixfold symmetry is the average over many small orthorhombic domains with orientation differing by 120° [55]. This is also the present case. Assuming molecular dimensions of 0.154 nm for CC bonds, 0.107 nm for CH bonds, 0.12 nm for the Van der Waals radius of H and 109° 28′ for all bond angles [56], the minimum enveloping cylinder diameter for an aliphatic chain is 0.516 nm, corresponding to a cross-sectional area per hcp chain of 0.23 nm^2.

All such paracrystalline lattice disturbances will lead to stress fields of the disclination quadrupole type. As shown in appendix C, it is possible to combine the NH and paracrystal theory to form a theory of lattices with independent random distributions of both disclination dipoles and quadrupoles. The resulting spot profile is the convolution of the spot profile due to dipoles only, with that due to quadrupoles only. Hence on this model the central shape of the peak, including the FWHM, is still determined by the dislocation density. When paracrystalline defects are present in significant numbers, the wings of the profile are power-law (as is the case in the Lorentz profile).

It is also possible to explain a non-Gaussian lineshape in terms of a non-equilibrium distribution of dislocations. It has previously been reported that the component of optical loss due to large-angle scattering in LB films of 22-tricosenoic acid has a square-law variation with the in-plane optical anisotropy, suggesting that variations of local 2-dimensional lattice orientation are the major cause of this scattering [18]. The present study indicates that dislocations are a plausible cause of these variations. There have been a number of reports [57] that the large-angle scattering in LB films of several different materials is not uniform, but is concentrated at certain points, and that the density of these light-scattering points varies systematically with position in the film [58] and deposition conditions [59]. Hence it is plausible that the dislocation density in the films displays macroscopic inhomogeneities. Clearly it is possible to modify the NH theory with a suitable statistical distribution of dislocation densities to explain the observed slower-than-Gaussian fall-off. Since spot smearing is also accompanied by a displacement of the spot centre towards the origin, this model also leads to an asymmetric profile, falling off more slowly on the side of the undeflected beam, although with the present best-fit parameters this asymmetry is undetectable.

5. Conclusions.

The diffraction pattern from a real two-dimensional crystal has been derived mathematically for three distinct cases where specific lattice defects occur with specific statistics. Each of the three cases has been proposed at some time to describe the organisation of monolayers or

smectics. The diffraction pattern to be expected from a Nelson-Halperin hexatic smectic has not previously been derived from first principles. The present treatment of the paracrystal is a significant improvement on previous attempts in that the strain pattern caused by the defects is in mechanical equilibrium.

The predictions of each of the three models have been compared to experimental patterns for LB films of two different aliphatic chain compounds, leading to the same conclusions for both materials. Using the aspect ratio criterion, the polycrystalline model could be rejected. The radial profile criterion provided a definitive refutation of the paracrystalline model but did not choose between the polycrystalline and NH models, each of which showed systematic error. Although the differences between the polycrystalline and NH models for the width variation criterion were comparable to the experimental error, this test favoured the NH model, and moreover the best fit to the polycrystalline model contained an internal contradiction. To sum up, the best agreement was achieved for the NH model of an interacting gas of dislocations, while the other two models had serious shortcomings.

Some discrepancies in the fit to the NH model remain, and two ways of improving it have been proposed for future investigation. However, independent of the fine details of interpretation, loosely bound dislocations have been demonstrated to be a major cause of broadening of the diffraction spots.

Acknowledgments.

This work was financed jointly by the Bundes Ministerium für Forschung und Technologie within the Ultrathin Polymer Film Project No. 03 M 4008 C 3, by the Deutsche Forschungsgemeinschaft within the Special Research Initiative SFB 262 on Nonmetallic Glasses, and by the Materials Science Research Center of the University of Mainz. The authors would like to thank Dr D. R. Nelson and Dr J. E. Riegler for useful discussions. Special thanks are due to Professor H. Möhwald for having initiated the project, and for his continued encourangement and support.

Appendix A.

Derivation of the polycrystalline scattering function.

In the normal concept of a polycrystalline material, individual grains are essentially strain-free perfect crystals, with no correlation between the orientations of neighbouring grains. When the selected diffraction area encompasses many grains, this always gives rise to a ring diffraction pattern, contrary to observation, and contrary to the optically observed long-range orientational order in LB films. Hence it is necessary to consider an unusual case in which, through some mechanism, neighbouring grains have highly correlated orientations. However, in order for the polycrystalline idea to make sense it must be assumed that there is no translational coherence from grain to grain, and that grain boundaries are randomly distributed.

The first step in the derivation of the scattering function is to calculate the Patterson function, or spatial correlation function of the material refractive index, from the assumed statistics of molecular position. In the following, point molecules with a delta-function refractive index profile will be assumed. For investigations of the lattice contribution to scattering, this is all that is required, and in any case the scattering function for real molecules can be readily derived from that for point molecules by well-known methods. Within a grain, the contribution to the autocorrelation function from a given spacing is equal to that for a perfect lattice. Since there is no phase coherence between grains, then if a grain boundary

separates the two points, the contribution to the autocorrelation function is constant and equal to the lattice density. As in the Poisson distribution, the probability that no grain boundary separates two points varies exponentially with the distance between them. Hence, if M is the 2×2 matrix formed by the unit cell vectors, then the Patterson function is given by :

$$P(R) = \text{Ш}_M(R) \,.\, \exp(-|R|/\xi) + \det M^{-1} \,.\, [1 - \exp(-|R|/\xi)] \,. \tag{A.1}$$

Appendix D defines the lattice comb function Ш_M (D8) and derives its Fourier transform (D.9) as well as that of e^{-r} (D.7). The Fourier transform of the overall Patterson function, i.e. the scattering function, is then readily derived to be :

$$S(K) = \det M^{-1} \,.\, [\text{Ш}_M^{T\,-1} - \delta] * 2\pi [1 + 4\pi^2 \xi^2 |K|^2]^{-3/2}, \quad |K| \neq 0 \,. \tag{A.2}$$

Hence apart from the small-angle scattering peak, the diffraction spots are all identical, with circular cross-section and Lorentzian profile (in the sense of power law asymptote — more precisely, Lorentzian to the power 1.5). The characteristic domain size ξ is related to the FWHM by :

$$\xi = \sqrt{2^{2/3} - 1}/(\pi \,.\, \text{FWHM}) \,. \tag{A.3}$$

Appendix B.

Derivation of the Nelson-Halperin hexatic smectic scattering function.

The system Hamiltonian is given by [26, 60] :

$$\left.\begin{aligned} H = {} & (2/\sqrt{3}\, a^2) \,.\, C \sum_i \{b_{i\rho}\, b_{i\rho}\} + \\ & + 4\pi A \cdot \sum_{i<j} \{-b_{i\rho}\, b_{j\rho} \ln (r_{ij}/a) + b_{i\rho}\, b_{j\sigma} (X_{i\rho} - X_{j\rho})(X_{i\sigma} - X_{j\sigma})/r_{ij}^2\} \end{aligned}\right\} \tag{B.1}$$

where $$r_{ij} = \sqrt{(X_{i\rho} - X_{j\rho})(X_{i\rho} - X_{j\rho})} \,.$$

This is a bilinear form in the Burgers vectors $b_{i\rho}$, which have the dimensions of length. i and j are lattice position labels, while ρ, $\sigma = 1, 2$ label the Cartesian components, and repeated suffixes imply summation using the Einstein convention. a is the nearest neighbour spacing of the hcp lattice, A is related to the Lamé elastic constants of the mechanically isotropic layer by :

$$A = \mu(\mu + \lambda)/\lambda/(2\mu + \lambda)$$

while $2C/\sqrt{3}$, the energy required to create a dislocation of smallest possible Burgers vector, depends in addition on the high-strain nonlinear elastic behaviour of the lattice. On physical grounds it is possible to say that, since most lattice points are not dislocated, then $C > kT$, while since the dislocations only interact weakly, then $Aa^2 < kT$.

In the Debye-Hückel approximation the expectation values of measurable parameters are calculated by allowing the amplitudes of the various Burgers vector components to vary continuously [26]. At thermal equilibrium all possible configurations of the b's contribute to measurable system parameters, with probability or weighting factor proportional to $\exp(-H/kT)$. This has the general form of a multivariate Gaussian distribution of the b's.

Since H commutes with translation, reflection and rotation, the matrix of the bilinear form is diagonalised by a choice of basis consisting of longitudinal and transverse plane waves of

dislocation density. The most convenient is the all-real Hartley basis. For a bilinear form, it is essential to define the amplitude of the basis elements : this may be conveniently taken to be 1 m.m^{-2} rms density. Explicitly, for the two basis elements with wavevector Q c.m^{-1}, the total Burgers vector δb of bad crystal contained in a small area δS centred on X is given to first order by :

$$\left.\begin{aligned} &\text{Longitudinal :} \\ &\qquad \delta b_\rho(Q, X) = Q_\rho/|Q| \,.\, \mathrm{cas}\ (2\,\pi Q_\sigma X_\sigma)\,.\,\delta S \\ &\text{Transverse :} \\ &\qquad \delta b_\rho(Q, X) = \varepsilon_{\rho\tau}\, Q_\tau/|Q| \,.\, \mathrm{cas}\ (2\,\pi Q_\sigma X_\sigma)\,.\,\delta S \end{aligned}\right\} \tag{B.2}$$

where cas $\vartheta = \cos\vartheta + \sin\vartheta$, and $\varepsilon_{\rho\sigma}$ is the unit antisymmetric matrix. Then the corresponding diagonal elements of H are proved in reference [26] to be given for a region of area S by :

$$\left.\begin{aligned} &\text{Longitudinal polarisation } (b \parallel Q) : \\ &\qquad h_{\mathrm{L}}(Q) = C\,.\,S\,. \\ &\text{Transverse polarisation } (b \perp Q) : \\ &\qquad h_{\mathrm{T}}(Q) = (C + A/|Q|^2)\,.\,S\,. \end{aligned}\right\} \tag{B.3}$$

Since there are no off-diagonal terms of the Hamiltonian matrix expressed in terms of the coefficients $\hat{b}$ of the Hartley basis, it follows that these coefficients are independent Gaussian random variables, with zero mean and variance $kT/2\,h$. Since $C > kT$, the vast majority of dislocations will have Burgers vector of length a, so that the total dislocation density n is given in terms of the plane wave amplitudes by :

$$\begin{aligned} n &= \frac{kT}{2} \cdot \iint \mathrm{d}^2Q : \left[\frac{1}{C} + \frac{|Q|^2}{A + C\,|Q|^2}\right] \\ &\approx \frac{kT}{C} \cdot \frac{2}{\sqrt{3}\,a^2} \quad \text{since} \quad Aa^2 \ll C\,. \end{aligned} \tag{B.4}$$

A point dislocation in a hcp lattice with Burgers vector b_ρ is well-known to produce the following displacement field u_ρ at a point located at distance r and azimuth ϑ from the dislocation [50, 61] :

$$u_\rho = \begin{bmatrix} \vartheta + \dfrac{\alpha}{2}\sin 2\vartheta & (1-\alpha)\ln r - \dfrac{\alpha}{2}\cos 2\vartheta \\ -(1-\alpha)\ln r - \dfrac{\alpha}{2}\cos 2\vartheta & \vartheta - \dfrac{\alpha}{2}\sin 2\vartheta \end{bmatrix}_{\rho\sigma} \cdot \frac{b_\sigma}{2\,\pi} \tag{B.5}$$

with $\alpha = (\mu + \lambda)/(2\,\mu + \lambda)$, μ and λ being the Lamé coefficients of the dislocation-free lattice, or alternatively $\alpha = 0.5/(1 - \nu)$, ν being the Poisson's ratio. It is of interest to note that this displacement field can be considered to be due to a disclination dipole [62] :

$$\left.\begin{aligned} &u_\rho = \Phi_{\rho,\sigma}\, \varepsilon_{\sigma\tau}\, b_\tau/2\,\pi \\ &\text{where} \\ &\Phi_1 + i\Phi_2 = (x + iy)[(1-\alpha)\ln r + i\vartheta]\,. \end{aligned}\right\} \tag{B.6}$$

The displacement field produced by a general longitudinal plane wave, say, should be derivable from that due to one with its wave vector parallel to x, by rotation. However direct

Fourier transformation of (B.5) to give the displacement field produced by the Hartley basis (B.2) does not have this property, due to the multivalued nature of ϑ and the asymptotic divergence of $\ln r$. The following displacement fields have the correct symmetries, and give the correct local lattice rotation. They have the variation in α expected for the Fourier transform of (B.6), i.e. due to all terms except the multivalued term ϑ, and can be derived from a stress field corresponding to a force $\mu \varepsilon_{\rho\sigma} b_\sigma / 2\pi$ on each dislocation b :

Longitudinal modes $(b \parallel Q)$:

$$u_\rho(Q, X) = \varepsilon_{\rho\sigma} Q_\sigma / 2\pi |Q|^3 . \operatorname{cas}(2\pi Q_\tau X_\tau)$$

Transverse modes $(b \perp Q)$:

$$u_\rho(Q, X) = (1 - \alpha) . Q_\rho / 2\pi |Q|^3 . \operatorname{cas}(2\pi Q_\tau X_\tau) . \qquad \text{(B.7)}$$

It should be noted that these fields are single-valued, like any plane wave field, and so represent the smoothly varying, commensurate, part of the total displacement field.

In order to derive the scattering function $S(K)$, the spatial correlation function or Patterson function $P(X)$ must first be calculated and then Fourier transformed [28]. In the present case the Patterson function is the sum of Gaussians, representing the probability distribution function of each perfect hexagonal lattice spacing Y distorted by the strain field. Since the $\hat{b}$'s are all real, independent random variables, the correlation matrix $C_{\rho\sigma}(Y)$ for the displacement of this lattice spacing is the sum of the contributions from each. In a coordinate system with unit basis vectors parallel and perpendicular to Y, it is readily expressed as :

$$C_{\rho\sigma}(Y) = \frac{kT}{C} \iint \mathrm{d}^2Q \cdot |Q|^{-4} \begin{bmatrix} \sin^2\varphi & 0 \\ 0 & \cos^2\varphi \end{bmatrix}_{\rho\sigma} \cdot \sin^2(\pi |Q \parallel Y| \cos\varphi) +$$

$$+ kT \cdot (1 - \alpha)^2 \cdot \iint \mathrm{d}^2Q \cdot \frac{|Q|^{-2}}{A + C|Q|^2} \cdot \begin{bmatrix} \cos^2\varphi & 0 \\ 0 & \sin^2\varphi \end{bmatrix}_{\rho\sigma} \cdot \sin^2(\pi |Q \parallel Y| \cos\varphi) \qquad \text{(B.8)}$$

with φ the angle between Q and Y, and with a range of integration over the first Brillouin zone of the hexagonal lattice, which is approximately a circle with radius $0.61/a$. The first integral (associated with longitudinal modes) diverges at the origin : the divergence can be eliminated by specifying a cutoff radius which may be interpreted as the reciprocal of the diffraction aperture. It is also permissible to approximate the final $\sin^2$ term by the square of its argument. Because of the divergence of the first term, the second integral associated with transverse modes may be neglected under most circumstances.

Hence the Patterson function is given by :

$$P(X) \approx \iint \mathrm{d}^2Y \cdot \mathrm{Ш}_M(Y) \cdot \frac{\exp\left[-\frac{1}{2} C^{-1}_{\rho\sigma}(Y)(X_\rho - Y_\rho)(X_\sigma - Y_\sigma)\right]}{2\pi \cdot \sqrt{\det C(Y)}} \qquad \text{(B.9)}$$

where

$$C_{\rho\sigma}(Y) = \frac{\pi \sqrt{3} \cdot na^2 \cdot \ln B}{8} \cdot (3\delta_{\rho\sigma}\delta_{\tau\upsilon} - 2\delta_{\rho\tau}\delta_{\sigma\upsilon}) Y_\tau Y_\upsilon ,$$

so that

$$\sqrt{\det C(Y)} = \frac{3\pi . na^2 . \ln B}{8} |Y|^2$$

B is the ratio of the diffraction aperture diameter to the lattice spacing, and M is the matrix formed by the unit-cell vectors of a dislocation-free lattice with the same orientation and lattice spacing as the smectic layer. $\text{Ш}_M(Y)$ is the comb function for this lattice, defined in equation (D.8).

The Fourier transform with respect to X of the integrand in (B.9) may be derived from the standard integral (D.9) :

$$S(K) \approx \iint \mathrm{d}^2 Y \,.\, \text{Ш}_M(Y) \,.\, \exp\left[2\,\pi i K_\sigma\, Y_\sigma - 2\,\pi^2 C_{\rho\sigma}(Y)\, K_\rho\, K_\sigma\right] \tag{B.10}$$

while the integral over Y can be handled using the identity (D.11) :

$$S(K) = \iint \mathrm{d}^2 L \cdot \frac{\text{Ш}_M^{\mathrm{T}-1}(L-K)}{\det M} \cdot \frac{\exp\left[-\frac{1}{2} C_{\rho\sigma}^{-1}(K)\, L_\rho\, L_\sigma\right]}{2\,\pi \cdot \sqrt{\det C\,(K)}} \,. \tag{B.11}$$

This is approximately a sum of Gaussians, each centred on one of the points of the reciprocal lattice. The scattering intensity contours are ellipses, with a ratio of major to minor axis of $\sqrt{3} = 1.73205..$ and the minor axis pointing in the direction of the origin. The radial full-width half-maximum (FWHM) divided by the distance to the origin is given by :

$$\begin{aligned} \frac{\mathrm{FWHM}}{r} &= \ln 2 \,.\, \sqrt{3\,\pi \,.\, \sqrt{3/4} \,.\, \ln B \,.\, na^{\,2}} \\ &= 2.5306 \,.\, \sqrt{\ln B \,.\, \tilde{n}} \end{aligned} \tag{B.12}$$

where $\tilde{n}$ is the normalised dislocation density per molecule.

Appendix C.

Scattering function for a paracrystal.

The essential difference between the displacement fields giving diffraction broadening in the NH model and those in a paracrystal is that the latter consists everywhere of good crystal in Burgers' sense, with zero circuit closure vector at each lattice point. Structures giving rise to such displacement fields are easy to imagine, for example vacancies, impurities, chain kinks, random crosslinks, or regions of different but near-commensurate molecular packing. The deformed lattice must be in mechanical equilibrium, so that the displacement field at all normal lattice points must satisfy the following differential equation :

$$\left.\begin{aligned} &(1-\alpha)\, u_{i,jj} + \alpha u_{j,ji} = 0 \\ \text{or in alternative notation :} \qquad & \\ &(1-\alpha)\, \nabla^2 \mathbf{u} + \alpha \nabla\,(\nabla \cdot \mathbf{u}) = 0 \,. \end{aligned}\right\} \tag{C.1}$$

This equation is satisfied both by the dislocation fields of (B.5) and by the disclination field of (B.6). In the present case the boundary conditions are different. It has been proved [62] that all solutions of (C.1) associated with point defects are sums of derivatives of the field due to a disclination. Clearly, the dominant long-range effects will be produced by the lowest order derivative : if dislocations are ruled out then disclination quadrupoles will dominate.

There are then three linearly independent possibilities a, b and c for the displacement field of a point defect, with radial and tangential components given by :

$$\begin{aligned} a_\rho &= r^{-1} \cdot \{-1, 0\}_\rho \\ b_\rho &= r^{-1} \cdot \{\cos 2\vartheta, -(1-\alpha)\sin 2\vartheta\}_\rho \\ c_\rho &= r^{-1} \cdot \{\sin 2\vartheta, (1-\alpha)\cos 2\vartheta\}_\rho . \end{aligned} \tag{C.2}$$

Physically, the a-field might be associated with a vacancy, the b-field with a crosslink parallel to the y-axis, and the c-field with a crosslink at 45° to both the x- and y-axes. Paracrystal statistics can be calculated from these displacement fields once the statistics of vacancies and crosslinks is defined. In the following, it will be assumed that the positions of these defects are uncorrelated. In an isotropic medium, the mean density of the b- and c-sources must be zero, and their variances must be equal.

As with dislocation density, it is useful to construct a complete set of eigenvectors of bilinear forms of vacancy and crosslink density commuting with translation, reflection and rotation. However here the displacement fields are much better behaved and there is no problem with Fourier transformation. The basis elements are plane waves, and for each wavevector Q there are three polarisations, corresponding to vacancies, crosslinks parallel to Q, and crosslinks at 45° to Q. For a density of each source type of cas $(2\pi Q_\tau X_\tau)$, the displacement fields are, respectively :

$$\begin{aligned} &(A)\ u_\rho = -Q_\rho/|Q|^2 \cdot \text{cas}\ (-2\pi Q_\tau X_\tau) \\ &(B)\ u_\rho = (1-\alpha) \cdot Q_\rho/|Q|^2 \cdot \text{cas}\ (-2\pi Q_\tau X_\tau) \\ &(C)\ u_\rho = \varepsilon_{\rho\sigma} Q_\sigma/|Q|^2 \cdot \text{cas}\ (-2\pi Q_\tau X_\tau) . \end{aligned} \tag{C.3}$$

The Patterson function may now be calculated in a similar way to the NH case. If there is a nonzero mean density of vacancies, the average position of the Patterson function peaks will be shifted : it is easy to show that this gives rise to a uniform shrinkage of the distances between the Patterson function peaks. The spot broadening depends only on the statistical variance of the plane wave amplitudes. Just as for (B.8), the correlation matrix for the lattice spacing Y is given, in a radial/tangential coordinate system, by :

$$\begin{aligned} C_{\rho\sigma}(Y) = \iint \mathrm{d}^2 Q \cdot |Q|^{-2} \cdot \sin^2(\pi |Q| |Y| \cos\varphi) \times \\ \times \{A + (1-\alpha)^2 B\} \cdot \begin{bmatrix} \cos^2\varphi & 0 \\ 0 & \sin^2\varphi \end{bmatrix}_{\rho\sigma} + C \cdot \begin{bmatrix} \sin^2\varphi & 0 \\ 0 & \cos^2\varphi \end{bmatrix}_{\rho\sigma} . \end{aligned} \tag{C.4}$$

In this case, the integrand is finite everywhere so that it is no longer appropriate to approximate to the $\sin^2$ term. However by expanding all trigonometric terms as sums of exponentials it can be seen that each term in the integral is the Fourier transform of a truncated $r^{-2} \cdot e^{im\vartheta}$ function, with $m = -2, 0$ or 2. The transform of $r^{-2} \cdot e^{im\vartheta}$ is derived in appendix D, equation (D.4).

Since the effect of local defects predominates, the assumption of a Gaussian distribution is not as good as in the NH case. However, it is still a reasonable assumption, and much more easily handled mathematically than more sophisticated alternatives. Hence equations (B.9) and (B.10) are valid for the paracrystal, with the correlation matrix now given by :

$$C_{\rho\sigma}(Y) = \beta \cdot \ln\ (|Y|/\xi) \cdot \delta_{\rho\sigma} + \gamma \cdot (2 Y_\rho Y_\sigma/|Y|^2 - \delta_{\rho\sigma}) \tag{C.5}$$

β, ξ and γ are constant parameters combining A, B, C, a and α. γ is a measure of the spot anisotropy. Its modulus is always less than that of β and it can have either sign. If isotropic defects dominate then the peak is preferentially broadened in a radial direction, while if crosslink-type defects dominate the broadening is tangential. The desired form of the scattering function is then obtained by applying identity (D.11). This gives the peak centred at reciprocal lattice point K as the Fourier transform of :

$$\left(\frac{r}{\xi}\right)^{-\beta|K|^2} . \exp\ \{\gamma\ .\ |K|^2 . \cos 2(\vartheta - \varphi)\} \tag{C.6}$$

where φ is the polar angle of K. It is readily seen from equation (D.3) that the radial variation of the diffraction spot is given by :

$$r^{\beta|K|^2-2} . \tag{C.7}$$

Hence within the critical radius $\sqrt{2/\beta}$ the peak intensity is infinite and the FWHM is zero, while outside this radius there are no peaks at all.

It can be seen that there is a marked parallelism between the derivations of this appendix, valid for disclination quadrupoles, and that of appendix B, valid for disclination dipoles. If both types of defect are present and independent of one another, then equations (B.9) and (B.10) are still valid, with the correlation matrix $C_{\rho\sigma}(Y)$ for the Patterson function peak at the point Y now equal to the sum of the matrices for the two defect categories separately. In the final step (B.11), each peak of the scattering function is the convolution of the peak due to quadrupoles alone, with that due to dipoles alone.

Appendix D.

Definitions and derivations.

This appendix contains definitions of special functions and notations used in the other appendices and indicates methods of evaluation for Fourier transforms and other integrals.

x and y are used ambiguously : either directly as variables, or as functions of two other variables, such that $x(a, b) = a$ and $y(a, b) = b$. However this should not lead to any difficulties. r and ϑ are similarly functions of two variables, conventionally defined in terms of x and y by :

$$\begin{aligned} x &= r . \cos\vartheta \quad & r &= \sqrt{x^2 + y^2} \\ y &= r . \sin\vartheta \quad & \vartheta &= \tan^{-1}(y/x), \quad \text{the principal value being in the range } -\pi \leqslant \vartheta < \pi \end{aligned} \tag{D.1}$$

The symbol $\mathfrak{F}$ is the Fourier transformation operator on functions of two variables :

$$\mathfrak{F}F(x, y) = \int^{\infty} \int F(k, \ell) . \exp\ \{2\pi i (kx + \ell y)\} . \mathrm{d}k\, \mathrm{d}\ell . \tag{D.2}$$

As in reference [28], the resulting frequencies k and ℓ have the units of cycles per unit x and y. This simplifies comparison with experimental work (the d-spacing is the length of a cycle, not a radian). In addition, in these units $\mathfrak{F}^2$ is the operation P of inversion through the origin, with no complicating factors of 2π.

The functions $r^{-n} . e^{im\vartheta}$ are especially important. A simple change of variable in the

integral (D.2) readily gives the transform apart from a multiplicative factor :

$$\left.\begin{aligned} \mathfrak{F}(r^{-n} \cdot e^{im\vartheta}) &= K_{mn} \cdot r^{n-2} \cdot e^{im\vartheta} \\ \text{where} \qquad K_{mn} &= \int_0^{\infty} dr : \int_0^{2\pi} d\vartheta : r^{1-n} \cdot e^{im\vartheta} \cdot e^{2\pi i r \cos\vartheta} . \end{aligned}\right\} \tag{D.3}$$

The coefficients K may be evaluated by direct integration to give :

$$K_{mn} = i^{-|m|} \cdot \pi^{n-1} \cdot \Gamma\left(1 - \frac{n + |m|}{2}\right) \Big/ \Gamma\left(\frac{n - |m|}{2}\right) . \tag{D.4}$$

This diverges in the interesting case $m = n = 0$. However since

$$\left.\begin{aligned} \ln r &= \lim_{n \to 0} (r^n - 1)/n \\ \mathfrak{F}(\ln r) &= -1/2\, \pi r^2 \\ \text{and inversely} \qquad \mathfrak{F}(r^{-2}) &= -2\pi \cdot \ln r . \end{aligned}\right\} \tag{D.5}$$

Now, $\dfrac{\partial\vartheta}{\partial x} = -r^{-1} \cdot \sin\vartheta$, valid even for the discontinuity at $\vartheta = \pm\pi$

$$\begin{aligned} -2\pi i r \cos\vartheta \mathfrak{F}\vartheta &= i r^{-1} \cdot \sin\vartheta \\ \mathfrak{F}\vartheta &= -\tan\vartheta / 2\pi r^2 . \end{aligned} \tag{D.6}$$

The Patterson function derived for the polycrystalline case has the form $\exp(-r)$. In 1D, the Fourier transform is the well-known Lorentzian. In two dimensions, the integral (D.2) expressed in polar coordinates may be evaluated by first integrating with respect to r from $-\infty$ to $+\infty$, and then using the substitution $t = \tan\vartheta$:

$$\mathfrak{F} e^{-r} = 2\pi \cdot (1 + 4\pi^2 r^2)^{-3/2} . \tag{D.7}$$

$\text{Ш}_M(Y)$ is the generalised comb function [63], consisting of a sum of delta functions located at each point of a Bravais lattice. The lattice is specified by the matrix M whose columns are formed by the unit cell vectors. The comb function is formally defined by :

$$\text{Ш}_M(X) = \sum_{Y \mid \forall \rho,\, M^{-1}_{\rho\sigma} Y_\sigma \in \mathbb{Z}} \delta(X - Y) . \tag{D.8}$$

The transform of Ш_M can be derived by transforming to a coordinate system in which M is the unit matrix. The one-dimensional unit comb function is its own transform :

$$\mathfrak{F}\text{Ш}_M = (\det M)^{-1} \ \text{Ш}_{M^{T-1}} . \tag{D.9}$$

The Fourier transform of the general Gaussian function is required to transform the Patterson function (B.9) into the scattering function (B.10) in the NH case, and for the corresponding step of the paracrystal case. It can be derived from the following standard integral [64] :

$$\iint d^2X \cdot \exp\left[A_\rho X_\rho - \frac{1}{2} B_{\rho\sigma} X_\rho X_\sigma\right] = \sqrt{\det (2\pi B^{-1})} \cdot \exp\left[\frac{1}{2} B^{-1}_{\rho\sigma} A_\rho A_\sigma\right] . \tag{D.10}$$

This is similarly proved by transforming to a coordinate system in which B is diagonal.

The following identity is required for the final derivation of the scattering function for both the NH and paracrystal theories :

$$\iint^{\infty} F(Y)\, G(Y)\, \mathrm{d}^2 Y = \iint^{\infty} \mathfrak{F}F(L)\, \mathfrak{F}G(-L)\, \mathrm{d}^2 L\,. \tag{D.11}$$

The left-hand side is the Fourier transform evaluated at zero frequency of the product function FG. The right-hand side is the convolution of $\mathfrak{F}F$ and $\mathfrak{F}G$ evaluated at zero offset.

References

[1] HAVINGA E., DE WAEL J., *Rec. Trav. Chim.* **56** (1937) 375.
[2] GERMER L. H., STORKS K. H., *J. Chem. Phys.* **6** (1938) 280.
[3] STEPHENS J. F., TUCK-LEE C., *J. Appl. Cryst.* **2** (1969) 1.
[4] LIESER G., TIEKE B., WEGNER G., *Thin Solid Films* **68** (1980) 77.
[5] BONNEROT A., CHOLLET P. A., FRISBY H., HOCLET M., *Chem. Phys.* **97** (1985) 365.
[6] PETERSON I. R., RUSSELL G. J., *Philos. Mag. A* **49** (1984) 463.
[7] PETERSON I. R., RUSSELL G. J., *Thin Solid Films* **134** (1985) 143.
[8] DEBYE P. J. W., *Ann. Phys.* **43** (1914) 49.
[9] FISCHER A., SACKMANN E., *J. Phys. France* **45** (1984) 517.
[10] GAROFF S., DECKMAN H. W., DUNSMUIR J. H., ALVAREZ M. S., *J. Phys. France* **47** (1986) 701.
[11] VAINSHTEIN B. K., *Structure Analysis by Electron Diffraction*, transl. ed. by E. Feigel and J. A. Spink (Macmillan, New York) 1964.
[12] PETERSON I. R., RUSSELL G. J., *Brit. Polym. J.* **17** (1985) 364.
[13] LIESER G., TIEKE B., WEGNER G., *Thin Solid Films* **68** (1980) 77.
[14] PETERSON I. R., *Brit. Polym. J.* **19** (1987) 391.
[15] PETERSON I. R., EARLS J. D., GIRLING I. R., RUSSELL G. J., *Mol. Cryst. Liq. Cryst.* **147** (1987) 141.
[16] HARRIS W. F., *Sci. Am.* **237** (Dec. 1977) 130.
[17] PETERSON I. R., *J. Mol. Electron.* **2** (1986) 95.
[18] PETERSON I. R., EARLS J. D., GIRLING I. R., BARNES W. L., *J. Phys. D* **21** (1988) 773.
[19] CARTER F. L., SIATKOWSKI R. E., WOHLTJEN H., Eds, *Molecular Electronic Devices* (North Holland Amsterdam) 1988.
[20] DORSET D. L., JAP B. K., HO M. H., GLAESER R. M., *Acta Cryst.* **A35** (1979) 1001.
[21] VOIGT-MARTIN I. G., DURST H., KRUG H., *Macromol.* **22** (1989) 595.
[22] VOIGT-MARTIN I. G., KRUG H., VAN DYCK D., *Phys. Rev.*, in press.
[23] PETERSON I. R., *J. Mol. Electron.* **3** (1987) 103.
[24] NELSON D. R., *Phys. Rev. B* **18** (1978) 2318.
[25] HALPERIN B. I., NELSON D. R., *Phys. Rev. Lett.* **41** (1978) 121.
[26] NELSON D. R., HALPERIN B. I., *Phys. Rev. B* **19** (1979) 2457.
[27] NELSON D. R., HALPERIN B. I., *Phys. Rev. B* **21** (1980) 5312.
[28] HOSEMANN R., BAGCHI S. N., *Direct Analysis of Diffraction By Matter* (North-Holland, Amsterdam) 1962.
[29] ZERNIKE F., PRINS J. A., *Z. Phys.* **41** (1927) 184.
[30] WARREN B. E., AVERBACH B. L., *J. Appl. Phys.* **21** (1950) 595.
[31] BRÄMER R., RULAND W., *Makromol. Chem.* **177** (1976) 3601.
[32] CRIST B., COHEN J. B., *J. Polym. Sci. Polym. Phys. Ed.* **17** (1979) 1001.
[33] PETERSON I. R., RUSSELL G. J., EARLS J. D., GIRLING I. R., *Thin Solid Films* **161** (1988) 325.
[34] FISCHER A., SACKMANN E., *J. Coll. Interface Sci.* **112** (1986) 1.
[35] REIMER L., Elektronenmikroskopische Untersuchungs- und Präparationsmethoden (Springer Berlin) 1967, p. 322.

[36] LAXHUBER L. A., ROTHENHÄUSLER B., SCHNEIDER G., MÖHWALD H., *Appl. Phys.* **A39** (1986) 173.
[37] ORTH H., FISCHER E. W., *Makromol. Chem.* **88** (1965) 118.
[38] ANDREWS E. H., VOIGT-MARTIN I. G., *Proc. R. Soc.* **A327** (1972) 251.
[39] VOIGT-MARTIN I. G., in KAUSCH H., Ed., Characterisation of Polymers in the Solid State, *Adv. Polymer Sci. Ser.* No 67 (Springer Verlag Berlin) 1984.
[40] CREWE A. V., ISAACSON M. S., ZEITLER E., in Advances in Structure Research by Diffraction Methods, W. Hoppe, R. Mason Eds. **7** (Springer Verlag Berlin) 1979.
[41] VOIGT-MARTIN I. G., DURST H., *Macromolecules* **22** (1989) 168.
[42] BONNEROT A., CHOLLET P. A., FRISBY H., HOCLET M., *Chem. Phys.* **97** (1985) 365.
[43] HUI S. W., PARSONS D. F., COWDEN M., *Proc. Nat. Acad. Sci. USA* **71** (1974) 5068.
[44] RIEGLER J. E., *J. Phys. Chem.* **93** (1989) 6475.
[45] PATERSON M. S., *J. Appl. Phys.* **23** (1952) 805.
[46] GAY P., HIRSCH P. B., KELLEY A., *Acta Metall.* **1** (1953) 315.
[47] MATUCHA K. H., FRANZBECKER W., WILKENS M., *Phys. Stat. Sol.* **33** (1969) 493.
[48] KUŽEL R., KLIMANEK P., *J. Appl. Cryst.* **21** (1988) 363.
[49] PEIERLS R. E., *Ann. Inst. Henri Poincaré* **5** (1935) 177.
[50] KELLY A., GROVES G. W., Crystallography and Crystal Defects (Longman London) 1970.
[51] INOUE T., YASE K., OKADA M., OKADA S., MATSUDA H., NAKANISHI H., KATO M., *Thin Solid Films,* in press.
[52] BIBO A. M., PETERSON I. R., *Thin Solid Films* **178** (1989), 81.
[53] PETERSON I. R., EARLS J. D., GIRLING I. R., RUSSELL G. J., *Mol. Cryst. Liq. Cryst.* **147** (1987) 141.
[54] GRUEN D. W. R., *J. Phys. Chem.* **89** (1985) 146.
[55] GRAY G. W., GOODBY J. W., Smectic Liquid Crystals : Textures and Structures (Heyden Philadelphia) 1984.
[56] WEAST R. C., CRC Handbook of Chemistry and Physics, 57th Ed (CRC Press Cleveland) 1976.
[57] WINTER C. S., TREDGOLD R. H., VICKERS A. J., KHOSHDEL E., HODGE P., *Thin Solid Films* **134** (1985) 49.
[58] BLODGETT K. B., LANGMUIR I., *Phys. Rev.* **51** (1937) 964.
[59] NOVAK V. R., *Mikroelektronika* **12** (1983) 181.
[60] Errata, *Phys. Rev. Lett.* **41** (1978) 519.
[61] FRIEDEL J., Dislocations (Pergamon Oxford) 1964.
[62] ESHELBY J. D., READ W. T., SHOCKLEY W., *Acta Metall.* **1** (1953) 251.
[63] IIZUKA K., Engineering Optics, 2nd Ed, *Opt. Sci. Ser.* (Springer Berlin) **35** (1986) 44-46.
[64] KENDALL M., STUART A., The Advanced Theory of Statistics, 4th Edn (Charles Griffin London) **1** (1977) 372-396.